Research Square

Preprints are preliminary reports that have not undergone peer review.
They should not be considered conclusive, used to inform clinical practice,
or referenced by the media as validated information.

Heat and Fluid Flow Modeling in Laser Powder Bed Fusion of Ti-6Al-4V: Insights from a Multi-Track Study Beyond Single-Track Analysis

Toufik Tamsaout

t.tamsaout@crnn.dz

Centre de Recherche en Nanosciences et Nanotechnologies

Karim Kheloufi

Centre de Recherche en Nanosciences et Nanotechnologies

Oum El Kheir Hadj Rahmoun

Centre de Recherche en Nanosciences et Nanotechnologies

El-Hachemi Amara

Centre de Recherche en Nanosciences et Nanotechnologies

Research Article

Keywords: Laser powder bed fusion, OpenFOAM, Computational fluid dynamics, Multitrack, overlap ratio, melt pool evolution

Posted Date: November 14th, 2026

DOI: https://doi.org/10.21203/rs.3.rs-11498997/v1

License: This work is licensed under a Creative Commons Attribution 4.0 International License.
Read Full License

Additional Declarations: No competing interests reported.

Heat and Fluid Flow Modeling in Laser Powder Bed Fusion of Ti-6Al-4V: Insights from a Multi-Track Study Beyond Single-Track Analysis

Toufik Tamsaout, Karim Kheloufi, Oum El Kheir Hadj Rahmoun and El-Hachemi Amara

Center for Research in Nanoscience and Nanotechnology (CRNN)
Nanophotonic, Plasmonic, and Nanoelectronics Research Division
Abdelhafid Ihaddadene Scientific and Technological Hub,
Mahelma Road, Sidi Abdallah, 16201 Algiers, Algeria
Email: t.tamsaout@crnn.dz

Abstract

Laser powder bed fusion (LPBF) is widely recognized for its capability in the fabrication of complex metal components. However, the high thermal gradients and rapid solidification associated with this process remain major challenges for controlling melt pool stability and microstructural evolution. In particular, the effect of overlap ratio between passes on transient thermal behavior during multi-tracks scanning has not yet been fully understood, due to the difficulty of experimentally characterizing the underlying thermal phenomena. This study presents a high-fidelity computational fluid dynamics model, developed using OpenFOAM framework, to examine the effect of the overlap ratio on the melt pool evolution of Ti-6Al-4V during the LPBF process. The model incorporates the physics of heat transfer, fluid flow, phase changes, and the moving laser heat source to predict transient temperature evolution and melt pool dynamics. Four overlap conditions (0%, 10%, 20%, and 30%) were systematically analyzed under identical processing parameters. The thermal histories were quantitatively evaluated through peak temperature, liquid lifetime, solidification time, cooling rate, and remelting behavior. Two computational approaches are explored: single-track modeling where the laser power and scan speed are the primary varying parameters, and multi-track modelling encompasses varying overlapping conditions (0 %, 10 %, 20 %, and 30 %). To validate the model, single track results were first compared with experimental data reported in existing literature. The results reveal that increasing the overlap ratio significantly enhances thermal accumulation, prolongs the duration above the liquidus temperature, reduces cooling rates, and promotes repeated remelting through more intense interaction between adjacent tracks. These thermal mechanisms generate a large melt pool zone while altering the local solidification conditions that govern microstructure formation. The proposed numerical model provides detailed insight into the thermal mechanisms governing the multi-track LPBF process and serves as a reliable tool for optimizing scanning strategies and overlap parameters, thereby improving process stability and the quality of additively manufactured Ti-6Al-4V parts.

Keywords: Laser powder bed fusion, OpenFOAM, Computational fluid dynamics, Multitrack, overlap ratio, melt pool evolution

1. Introduction

Selective laser melting—also known as laser powder bed fusion (LPBF)—is a category of powder bed additive manufacturing processes in which a high-power, focused laser scans across successive thin layers of metal powder [1]. The laser selectively melts and fuses the material, enabling the layer-by-layer fabrication of three-dimensional parts. This technique is notable for its ability to produce highly complex geometries directly from digital models without requiring dedicated tooling or extensive post-processing [2].

Since the mid-2000s, LPBF has evolved from a rapid prototyping method into a qualified manufacturing process [3-4] for safety-critical applications in sectors such as aerospace [5], biomedical engineering [6], automotive and energy [7]. Commonly processed materials include Ti-6Al-4V, Inconel 718, and 316L stainless steel. The thermal conditions within the LPBF melt pool are extremely intense. Power densities on the order of 10^6–10^8 W/m² are concentrated into a laser spot typically 50–100 μm in diameter, moving at scan speeds between 0.1 and 4 m/s. This results in rapid cooling rates of 10^4–10^6 K/s and temperature gradients exceeding 10^6 K/m [8]. Such an environment gives growth to complex physical phenomena as surface tension gradients generate Marangoni convection [9], redistributing heat and matter within the melt pool, while metal vaporization induces a recoil pressure that depresses the liquid surface [10].

At high energy input, the melt pool can form a deep “keyhole” cavity that increases laser absorption through multiple reflections. However, this keyhole is unstable due to complex fluid flow and pressure–surface tension interactions, leading to trapped vapor bubbles during solidification [11]. These bubbles create spherical porosity beneath the surface, which degrades fatigue performance, making accurate prediction crucial for process optimization and part reliability [12]. Direct experimental observation of melt pool behavior in LPBF is highly challenging due to the extremely short time scales (on the order of microseconds) and small spatial scales (tens of micrometers). As a result, numerical modelling has become an essential tool for investigating the underlying physics of these processes offering varying levels of physical detail. [13–17]. Some models focus only on thermal behavior, treating the material as a continuous medium and neglecting particles and porosity [18]. However, capturing the influence of the powder bed requires resolving individual particles with appropriate mesh refinement.

Over the past decade, advanced multi-physics models have been developed to simulate melt pool evolution, keyhole behavior, and pore formation under both single-track and multi-track scanning conditions. When coupled with discrete element method (DEM) for powder and ray-tracing for laser absorption, these high-fidelity but computationally intensive simulations help reveal pore formation mechanisms and keyhole dynamics [19]. Khairallah et al. [20] used a high-fidelity arbitrary Lagrangian–Eulerian (ALE) -based, powder-scale model of 316L stainless steel LPBF process, incorporating recoil pressure, Marangoni convection, VOF free-surface tracking, and laser ray tracing. It showed that the coupled, temperature-dependent interaction between recoil pressure and Marangoni flow controls melt pool stability and defect formation.

The authors [21] extended multi-physics modeling to nanosecond-scale transient effects, showing that

spatter particles deposited ahead of the scan path can disturb the powder bed and initiate pore formation in later layers. Bayat et al. [19] developed a high-fidelity CFD model (implemented in Flow-3D) for single-track Ti6Al4V in L-PBF to investigate how laser power influences porosity formation. Their results showed that once a keyhole forms, laser rays become trapped within the cavity walls, undergoing multiple reflections that significantly increase energy absorption and heat transfer from the laser beam. Haodong Chen et al. [22] used a CFD–DEM multi-physics model (Flow-3D) to study the formation of end-of-process depression (EOPD) in LPBF, showing that reducing laser power near the end of the track can effectively mitigate this defect.

Chouhan et al. [23] combines experiments and DEM– OpenFoam simulations to study how melt pool flow behavior influences the surface morphology of single tracks in Laser Powder Bed Fusion (LPBF). They conclude that Track surface quality in LPBF is directly controlled by melt flow behavior, achieving stable and uniform flow through optimized process parameters is essential for smooth surfaces and defect-free tracks.

The overlap percentage between adjacent scan tracks was identified by many research papers to plays a critical role in achieving a dense microstructure, uniform melt pool behavior, and improved mechanical properties of the fabricated component. For example, Thongpron et al. [24] used CFD-based simulations to study how hatch spacing (overlap between adjacent scan tracks) affects surface roughness and melt pool behavior in SLM of Ti-6Al-4V, finding that excessive overlap destabilizes melt flow and leads to uneven surfaces. Chen Liu et al. [25] combines numerical simulation and experiments to investigate the effect of melt track overlap rate in selective laser melting of Ti-6Al-4V. The results show that the overlap rate strongly affects porosity, microstructure, and mechanical properties. The primary objective of this study is to investigate the behavior of melt pools and heat transfer laser melting of Ti-6Al-4V powder layer by understanding the effects of key process parameters.

For that purpose, a coupled CFD/DEM simulation of the powder laser melting process was built for. OpenFOAM® is an open-source computational fluid dynamics (CFD) software package that provides a wide range of built-in solvers for different applications. It is freely available and allows users to customize and extend the code to meet their specific needs, unlike proprietary software that is restricted to fixed functionalities. The DEM simulation represents powder distribution (diameter and particles positions), while the CFD simulation provides information on melt flow dynamics and heat transfer during melting and solidification.

In the first step, the simulation of single-track melting was at first modeled, and the results compared and validated with experiment results from previous work of AJI. Bagasol et al [26]. Then, the model was extended for modelling the multi-tracks melting to examine the influence of the hatch spacing (overlapping percentage) parameter on melt pool geometry, pore formation, and the impact of heat accumulation on melt pool behavior.

2. Mathematical model

A computational fluid dynamics (CFD) calculation, using the C++ open-source CFD toolbox called Open

Field Operation and Manipulation (OpenFOAM®), has been carried out to simulate the interaction between laser heat source and the Ti-6Al-4V powder material. All interfacial forces present in the process have been taken into account and simulated; these include surface tension (capillary force), Marangoni's flow (thermocapillary force), recoil pressure, drag force due to solid/liquid transition via Darcy's term, and buoyancy force (Figure 1). The energy dissipation in the mushy zone during melting, and heat loss due to evaporation, conduction, convection and radiation have been simulated in this work. The volume-of-fluid methodology has been used to simulate the evolution of the liquid/gas interface.

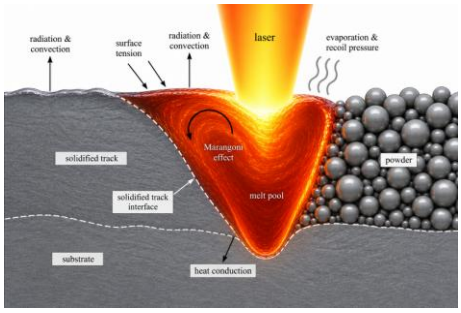


Figure 1: Main physical phenomena in the melt pool region during LPBF

2.1 Powder bed generation

In order to generate the powder bed, a discrete element method (DEM) model was used to simulate the free surface of the powder. To simulate the random packing of powder particles (assumed to be perfectly spherical) deposited onto a solid substrate, the powder particles were dropped freely on the substrate due to the gravitational force. Particle interactions were governed by contact forces between particles and gravitational forces, while their trajectories were determined by solving Newton's second law of motion. Particle–particle and particle–substrate contact interactions were modeled using the Hertz–Mindlin (no-slip) contact model, which accurately describes the normal and tangential contact forces during particle collisions. The resulting geometrical configuration of the deposited powder layer (radius and center coordinates of each particle) was then exported to OpenFOAM® [20] to be used as the initial condition for the subsequent melt pool dynamics simulation.

2.2 Heat transfer and melt flow dynamics

Assuming The melt pool to be incompressible, laminar, and Newtonian fluid, the governing equations of mass and momentum conservation are described as:

$$\vec{\nabla} \cdot \vec{v} = 0 \tag{1}$$

$$\frac{\partial(\rho\vec{v})}{\partial t} + \vec{v} \cdot \vec{\nabla}(\rho\vec{v}) = -\vec{\nabla}p + \vec{\nabla} \cdot \left(\mu\vec{\nabla}\vec{v}\right) + \rho_l \vec{g}\beta(T - T_l) + S_D + S_I \tag{2}$$

where $\vec{v}$ is velocity vector, t is time, p is the pressure, g is the gravity acceleration, μ is the mixture viscosity, ρ is the density of liquid metal, β is thermal expansion coefficient (Boussinesq approximation

of buoyancy) and Tl is the liqidus temperature.

In Eqn. 2 SD is the damping term in the mushy zone (Darcy's term) and is given by,

$$S_D = K_c \left[\frac{(1-f_l)^2}{f_l^3+b}\right] \cdot \vec{v} \quad (3)$$

where Kc is the mushy zone constant, fl fraction of liquid metal, and b is a small value to avoid division by zero.

The presence of a free surface in the melt pool necessitates the introduction of an additional equation to describe the evolution of the vapor interface. A conventional Volume-of-Fluid (VOF) approach is adopted in this study, in which the fluid volume fraction, F, is governed by the following conservation equation:

$$\frac{\partial F}{\partial t} + \vec{\nabla}.(F\ \vec{v}) = 0 \quad (4)$$

The final term Fs on the right-hand side in Eqn. 3.24 represent surface (interfacial) forces acting at the metal/gas interface. Three forces act on the interface, surface tension Fst, Marangoni force FM and recoil pressure Pr. These surface forces are included as volumetric source terms using continuous surface force model [Brackbill] and the cell phase gradient field $|\vec{\nabla}F|$:

$$S_I = \left\{\vec{F}_{st} + \vec{F}_M + \vec{P}_r\right\} \cdot \left|\vec{\nabla}F\right| \frac{2\bar{\rho}}{\rho_m+\rho_g} \quad (5)$$

and are expressed as:

$$\vec{F}_{st} = \sigma\kappa\vec{n} \quad (6)$$

$$\vec{F}_M = \frac{d\sigma}{dT}(\vec{\nabla}T - (\vec{n}\cdot\vec{\nabla}T)\vec{n}) \quad (7)$$

$$\vec{P}_r = 0.54P_a \exp(\frac{ML_v}{R}\frac{T-T_v}{TT_v})\vec{n} \quad (8)$$

where σ Is surface tension coefficient of metal at the melting point (solidus temperature), A is the surface tension gradient, P0 is ambient pressure, Lv is the latent of vaporization, Tv is the evaporation temperature, R is the universal gas constant, and M is the molar mass. The term $\frac{2\bar{\rho}}{\rho_m+\rho_g}$ is used here to redistribute the interfacial force towards the heavier metal phase in order avoid spurious currents (high acceleration flow) in the gas phase.

The unit normal vector $\vec{n}$ and surface curvature κ of metal/gas interface can be expressed as:

$$\vec{n} = \frac{\vec{\nabla}F}{|\vec{\nabla}F|} \quad (9)$$

$$\kappa = -\vec{\nabla} \cdot \vec{n} \quad (10)$$

The equation for energy conservation can be expressed in terms of enthalpy h as:

$$\rho \frac{\partial h}{\partial t} + \rho \vec{v} \cdot \vec{\nabla} h = \vec{\nabla} \cdot \left(\overrightarrow{k \nabla T}\right) - L_m \frac{\partial}{\partial t}(\rho f_l) + Q_{laser} - Q_{loss} \quad (11)$$

The total enthalpy of the material (h) is expressed as the sum of an integral of specific heat cp(T) and a latent heat contribution:

$$h(T) = \int_0^T c_p(T) dT + f_l(T).L_m \quad (12)$$

Using the approach outlined by Voller [43], a linear variation of liquid fraction with temperature in the mushy region is assumed as:

$$f_l(T) = \begin{cases} 0 & if\ T < T_S \\ \frac{T-T_S}{T_L-T_S} & if T_S \le T \le T_L \\ 1 & if\ T > T_L \end{cases} \quad (13)$$

To model the heat input due to laser absorption by the material and heat losses due to convection, radiation and vaporization, two source terms, Q_{laser} and Q_{loss} are incorporated into the energy conservation equation (Eq. 3) and are defined as follows [19, 23]:

$$Q_{laser} = \frac{2AP}{R_b^2} exp\left(-\frac{(x-x_0)^2+(y-y_0-Vt)^2}{R_b^2}\right) \left|\vec{\nabla}F\right| \frac{2\rho c_p}{\rho_m c_{pm} + \rho_g c_{pg}} \quad (14)$$

The terms A, P, Rb and V represent the laser absorptivity, the power, the beam radius, and the scanning speed, respectively, and (x, y) is the cell coordinate. The factor ($2\rho C_p/\rho_m Cp_m+\rho_g Cp_g$) is used to redistribute the heat input towards the metal phase (region of higher ρC_p).

$$Q_{loss} = \left[h_c\left(T - T_{ref}\right) + \varepsilon\, \sigma_s\left(T^4 - T_{ref}^4\right) + Q_{ev}\right] \left|\vec{\nabla}F\right| \frac{2\rho c_p}{\rho_m c_{pm} - \rho_g c_{pg}} \quad (15)$$

where h_c is the convection coefficient, T_{ref} is the reference temperature, σ_s is the Stefan–Boltzmann constant, e the emissivity, and Q_{ev} is the heat lost due to evaporation and is expressed as:

$$Q_v = 0.82 \frac{L_v}{\sqrt{2\pi MRT}} P_a \exp\left(\frac{L_v}{R} \cdot \frac{T-T_v}{TT_v}\right) \quad (16)$$

2.3. Absorptivity model

When a laser beam with total energy of P interacts with material, part of its energy is absorbed by the

material for a fraction equal to its absorptivity (a). In the present work, the absorptivity of the target material is described by Fresnel equations. For a light beam falling on the material interface at an incident angle θ, the absorptivity is equal to:

$$\mathrm{A}(\theta) = 1 - \frac{1}{2}\left(\frac{1+(1-\varepsilon\cos\theta)^2}{1+(1+\varepsilon\cos\theta)^2} + \frac{\varepsilon^2-2\varepsilon\cos\theta+2\cos^2\theta}{\varepsilon^2+2\varepsilon\cos\theta+2\cos^2\theta}\right) \quad (17)$$

and the reflectivity is simply calculated as (1- A). In Eq. (17), the absorptivity, A, is a function of the incident angle θ and of the laser-dependent and material-dependent quantity ε calculated using laser absorption data at normal incidence (θ=0). In our case, ε=0.2 for for Ti6Al4V alloy [14].

2.4. Multiple laser reflection model with ray-tracing method

To calculate the multiple reflections of the laser beam on the complex-shaped and time-varying surface, the laser beam is decomposed into a sufficient number of bundles of sub-rays each carrying a part of the beam energy as presented in figure 2.

The ray traversed cell by cell along its direction. If the ray reached a cell with a non-zero Volume fraction, the intersection points of the ray and the interface is determined and the ray tracing model calculates the incident angle and the heat exchange between the ray and the cell. The new direction of the reflected ray is calculated by the following geometrical relationship:

$$\vec{R}_0 = \vec{I}_1 = \vec{I}_0 - 2(\vec{I}_0 \cdot \vec{N}_0)\vec{N}_0 \quad (18)$$

where$\vec{R}_0$ is the reflected direction vector and $\vec{N}_0$ is the outward normal vector at the reflection points. The absorptivity of each ray at each interaction event is calculated using the Fresnel equations (see next section).

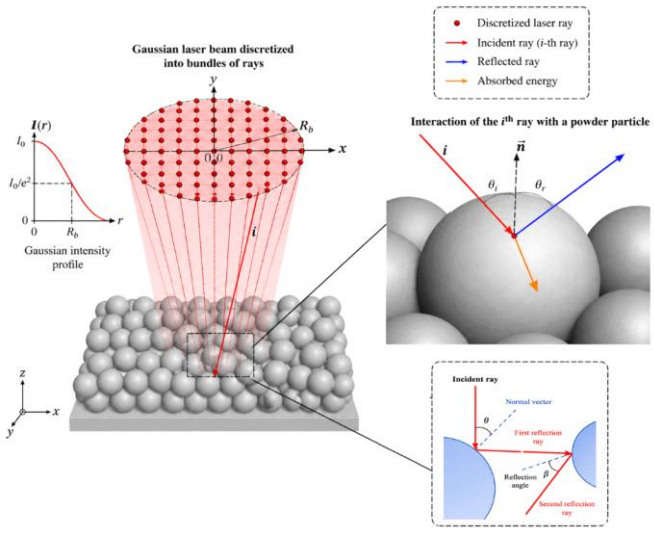


Figure 2: Multi-reflections of laser beam decomposition

3. Numerical model

3.1. Computational domain and mesh

The computational domain consists of a substrate, a powder-bed layer deposited on its upper surface, and the surrounding Argon gas region. In this study we use two computational domains, the first is used for single track simulations to validate the model whose dimensions are 1600 × 300 × 350 μm^3, including a substrate thickness of 200 µm and a powder-bed thickness of 80 µm, the second one is used for the multitrack simulations with dimensions of 1500 × 500 × 270 μm^3, including a substrate thickness of 150 µm and a powder-bed thickness of 60 µm. The domain was selected sufficiently large to minimize the influence of the external boundaries on the thermal field while resolving the laser–powder interaction region.

The powder bed was explicitly represented using spherical particles with a size distribution characterized by D10 = 21 µm, D50 = 32 µm, and D90 = 48 µm. The computational domain was discretized using a three-dimensional finite-volume mesh with a minimum Hex cell size of 5 µm resulting in approximately 1.5 million cells (figure 3). The laser heat source was represented by a Gaussian distribution with a nominal beam diameter of 80 µm for the validation model and 60 µm for the multitrack simulation.

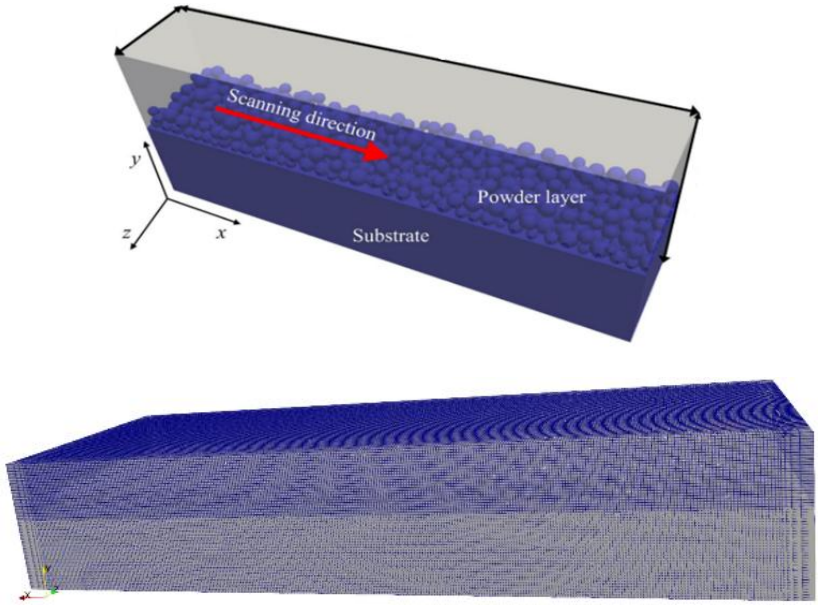


Figure 3: Computational Mesh Domain

3.2. Process parameters

3.2.1. Single-track parameters

Nine single-track simulations T1 to T9, were performed to evaluate the capability of the developed numerical model to reproduce the numerical and experimental results reported by Bagasol et al [26]. The laser power and scanning velocity were varied between the cases, whereas the powder-bed configuration and laser beam diameter were kept unchanged. The processing conditions adopted for the nine cases are summarized in Table 1 below.

Table 1. Laser processing parameters used for the single-track simulations.

Track N°	Laser Power (watt)	Scan Speed (mm/s)
T1	300	1333
T2	350	
T3	400	
T4	450	
T5	500	
T6	400	2000
T7		1600
T8		1142
T9		1000

3.2.2. Multi-track parameters

The multi-track simulations were performed to investigate the effect of inter-track overlap on the thermal history and melt-pool evolution. The hatch spacing H_S is defined as the centre-to-centre distance between two consecutive tracks. The overlap ratio O_r is defined as

$$O_r = \left(1 - \frac{H_s}{2\,R_b}\right) \times 100 \tag{19}$$

where R_b is the spot laser radius track. Therefore, increasing O_r corresponds to decreasing the distance between adjacent tracks and consequently increasing the spatial interaction between successive melt pools. Four overlap ratios were considered 0%, 10%, 20% and 30%. The corresponding hatch spacing H_S values were 60, 54, 48, and 42 µm, respectively. For all multi-track simulations, the laser power and scanning velocity were fixed at 170 W and 1200 mm s^{-1}, respectively. An inter-track delay of 50 µs was introduced between consecutive laser passes to account for the thermal evolution occurring between two successive scans. Five tracks were simulated for the 0% and 10% overlap conditions, while six tracks were considered for the 20% and 30% overlap conditions.

3.3. Model parameters

The mushy zone constant is generally considered as a model parameter and is chosen arbitrarily, as illustrated by the work of Katagiri et al. [27], who investigated its influence on the evolution of the melt pool. In the present study, this constant was defined using an assumption relationship based on the material density as K_c = 1000 ρ. This formulation offers a physical approach to select the mushy zone constant depending on the material properties used in the simulation, while avoiding the use of an arbitrary value. It provides a systematic basis for defining this parameter and could serve as a useful method for its determination in future studies.

The material used in this study is Ti-6Al-4V alloy thermophysical properties were obtained from the literature and implemented consistently in the model [19, 20]. The simulation for each case takes about 180–250 h to finish in a workstation with an Intel Core i7-13900K processor (24 logical threads) and RAM of 32Go.

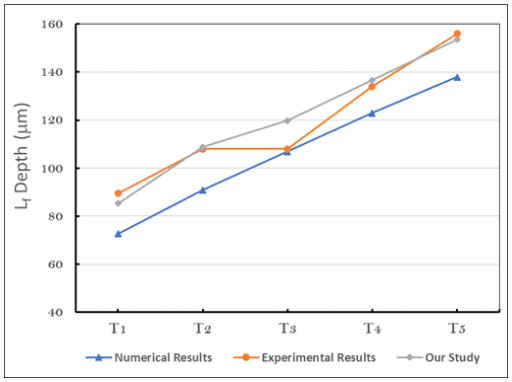
4. Model validation

To validate the developed laser powder bed fusion model and determine its accuracy, the predicted results was compared with both numerical and experimental results reported by Bagasol et al. [26] for Ti-6Al-4V

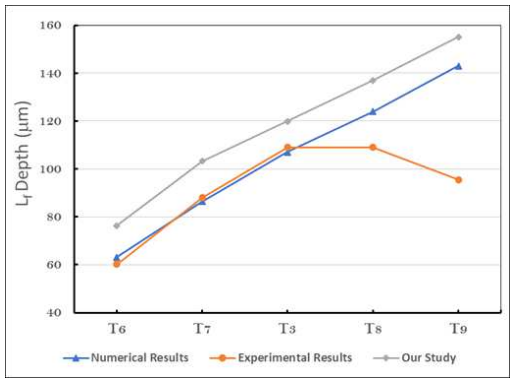
alloy. We study to the evolution of melt pool depth under different laser power and scanning speed, since this parameter remains one of the most sensitive indicators of thermal-fluid prediction accuracy in laser powder bed fusion simulations. The comparison concerns the evolution of the melt pool depth for nine single-track processing conditions (T1 to T9) applied to Ti-6Al-4V alloy. We have specially chosen this study because the authors present a comprehensive investigation of the experimental and numerical aspects of single-track formation, focused, in particular, the hydrodynamic behaviour of the molten pool by varying laser power at a constant scanning speed, as well as the effect of varying scanning speed under constant laser power.

The parameters used in the experiments and numerical study are the same as those used in the present model are listed in Table 1. Figure 4 show a quantitative comparison between our numerical results and those given by Bagasol & al [26] of the liquid fraction depth in nine (9) cases.

The first curve (figure 4-a) shows the evolution of the liquid fraction Depth in function of Laser Power T1 to T5 cases, at constant scanning velocity (1333mm/s) and the second one (figure 4-b) shows the variation of the Lf depth according to the scanning velocity at a constant laser power(400Watt) (T6 to T9 and T3).



a. Effect of Laser power on melt pool depth



b. Effect of scanning speed on melt pool depth

Figure 4: Quantitative comparison of our model results and Bagasol et al. ones [26]

The curves illustrate how the geometry of the melt pool depth, varies with laser power and scanning velocity. It is evident that, at a constant scanning speed (figure 4-a), increasing the laser power results in a deeper melt pool. On the other hand, when the laser power is held constant, reducing the scanning velocity leads to an increase in melt pool depth. For instance, at a scanning velocity of 1333 mm/s, the melt pool depth increases from 86 µm to 155 µm as the laser power rises from 300 W (T1) to 500 W (T5), as shown in

Figure 4-b, exceeding 2.5 times the powder layer thickness. Such a deeper remelting zone promotes stronger and denser metallurgical bonding. In contrast, at a higher scanning velocity of 2000mm/s, a shallower depth of approximately 76 µm is obtained at a laser power of 400Watt (T6), indicating that the heat input is insufficient to achieve dense bonding with the underlying layer.

The comparison shows that the present model achieves a closer agreement with the experimental measurements than the numerical results presented by Bagasol et al. [26]. This improved concordance can be attributed that our model takes into account Fresnel absorption, allowing the absorption coefficient to vary with incident angle and material state, rather than assuming a constant value as used by Bagasol et al. In addition, the current model includes the multiple reflections of the laser beam within the evolving keyhole, which improves energy deposition in deeper regions of the melt pool. These factors collectively contribute to make the developed model more accurate which leads us to conclude that the model is validated and can properly predict of Selective Laser Melting parameters.

5. Results and Discussion

5.1. Analysis of the Numerical results for one track simulation

5.1.1. General evolution of melt pool depth and keyhole penetration

The numerical results presented in Figures 5, 6 and 7 show the temporal evolution of the liquid fraction depth and keyhole penetration depth for the nine cases (T1 to T9) To ensure a clear and concise presentation, case T1 is presented in detail in Figure 5, while the corresponding results for cases T2 to T9 are presented as grouped and reduced-size figures to facilitate general comparison while avoiding unnecessary repetition in figure 6 for melt pool depth and figure 7 for keyhole depth.

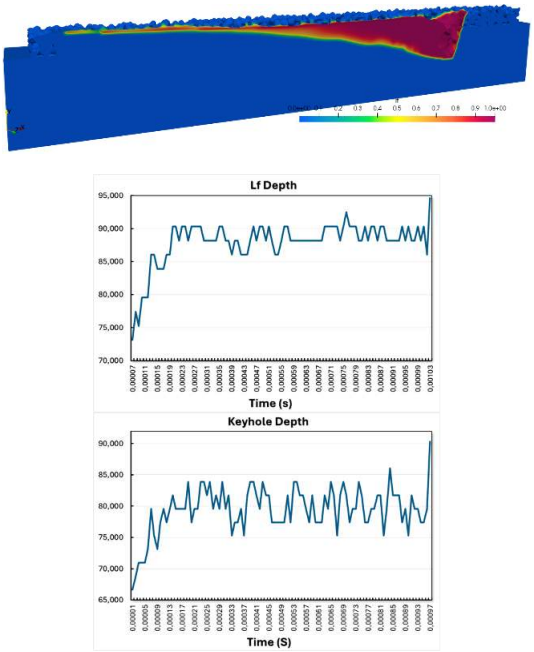


Figure 5: Transient melt pool and keyhole depths evolution for T1 case

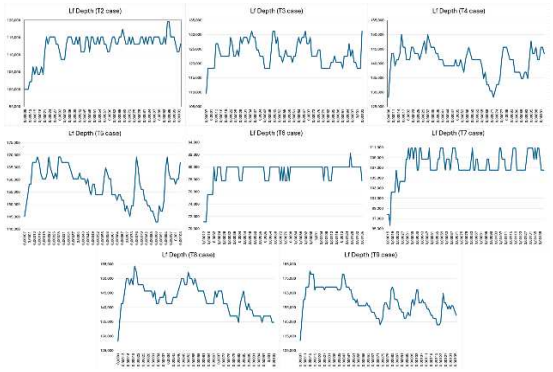


Figure 6: Transient melt pool depth evolution for T2 to T9 cases

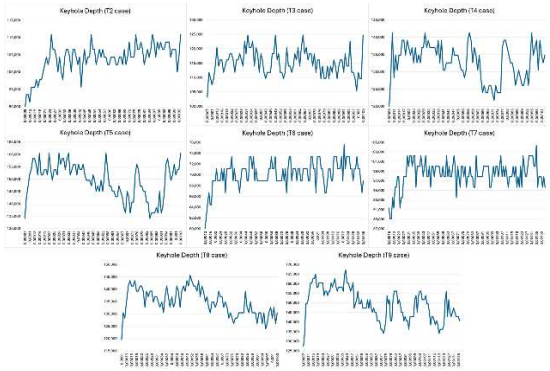


Figure 7: Transient keyhole depth evolution for T2 to T9 cases

During laser irradiation, the liquid fraction depth increases rapidly as energy is absorbed by the powder bed. Once the local temperature exceeds the liquidus temperature of Ti-6Al-4V, melting begins and the molten pool depth progressively increases. For all nine cases, the liquid fraction depth remains greater than the keyhole penetration one. This behavior is physically consistent since keyhole formation requires additional energy for vaporization and sufficient recoil pressure to develop a stable vapor cavity. In Case T1, for example, the liquid fraction depth is approximately about 110 µm, while the keyhole depth reaches 95 µm, illustrating the keyhole formation.

Cases T2 and T3 show a deeper melt pool and keyholes than T1, with T3 reaching approximately 155 µm for the liquid fraction depth and 146 µm for the keyhole. These results indicate a transition from stable to unstable keyhole regime as the process energy increases. This explanation is in excellent agreement with the results of Bagasol et al. [26], who reported that higher laser power improves melting pool penetration through increased thermocapillary convection and longer time interaction.

5.1.2. Influence of Laser power

The cases T1 to T5 correspond to the increasing laser powers from 300 W to 500 W with maintaining scanning speed constant. The numerical data show a constant increase of melt pool depth from T1 to T5 (T1 ≈ 85 µm, T2 ≈ 109 µm, T3 ≈ 120 µm, T4 ≈ 137 µm and T5 ≈ 154 µm), this evolution is entirely consistent with the physics mechanism governing SLM processing.

Increasing laser power produces a coupled effects that increase melt pool dimensions. Higher absorbed heat flux improves the local temperature and thermal gradients, while a higher recoil pressure enhances melting pool flow and promotes deeper keyhole penetration. At the same time,

intensified Marangoni convection redistributes heat within the molten pool, increasing both its depth and width.

The evolution of the melt pool depth with laser power, indicates that in keyhole-mode, recoil pressure and Marangoni convection become dominant, so even small increases in power lead to excessively larger penetration depths. These results are consistent with those of Ransenigo et al. [29], who reported that melt pool morphology becomes highly sensitive to laser power during keyhole formation. Furthermore, comparison with the experimental measurements of Bagasol et al. [26] demonstrates good overall agreement, with acceptable deviations considering the high sensitivity of laser powder bed fusion to absorptivity, powder characteristics, and vaporization modeling.

5.1.3. Influence of Scanning speed

The cases T3, T6 to T9 correspond to the increasing scanning speed while maintaining constant laser power. The numerical results show that reducing scan speed produces deeper melt pools (T6 ≈ 76 µm, T7 ≈ 103 µm, T3 ≈ 120 µm, T8 ≈ 137 µm and T9 ≈ 155 µm)

This mechanism is physically expected because reducing scan speed increases the interaction time between the laser beam and the material. Consequently, more thermal energy is deposite, increasing the local energy density. Then, the thermal diffusion time becomes sufficiently large to allow deeper heat penetration into the powder bed and the substrate. Simultaneously, the cooling rate decreases, promoting stronger melt pool accumulation, which increases significantly the melt depth. This leads to the onset of unstable keyhole behavior.

Such behavior is coherent with the benchmark study reported by Samaei et al. [30], where decreasing scan speed produced stronger keyhole oscillations, higher laser absorption coefficient and increased of the apparition of pores.

As shown above, compared with other previously published studies, the present numerical results provide strong evidence supporting the physical validity of our developed OpenFOAM model. These results further support the previous model validation which demonstrated that the numerical predictions consistently follow the same overall tendencies observed in both the experimental data and the numerical simulations reported by Bagasol et al. [26]

At high laser power, the present model slightly overpredicts melt depth relative to experiments. This behavior is common in CFD simulations of laser powder bed fusion because of existence of several mechanisms difficult to model such as powder denudation and spatter ejection which influence melt pool stabilization. Despite these limitations, the global agreement remains scientifically good and the model reproduces the correct behavior of the melt pool evolution.

5.2. Melt Depth and spatio-temporal temperature evolution during multi-track study: effect of the overlap ratio / hatch spacing

To study the thermal behavior during the multi-tracks LPBF process, two parameters were analyzed with varying the overlap ratio: the melt pool depth and the transient temperature. The temperature was recorded over time at three characteristic points located at the substrate-powder interface (top

face of the substrate) on the central plane perpendicular to the scanning direction. This configuration allows a consistent comparison between the different overlaps while precisely measuring the heat transfer from the melt pool to the substrate.

For each overlap ratio (0%, 10%, 20%, and 30%), the temperature was recorded throughout the simulation, covering all laser passes and the 50 µs cooling intervals between two consecutive scans. The resulting temperature profiles thus describe not only the direct heating generated by the laser beam, but also the successive heating induced by neighboring passes, enabling a quantitative analysis of the progressive heat accumulation, remelting phenomena, and solidification behavior throughout the multitrack process. The simulation was performed using a laser power of 170 W, a scanning speed of 1200 mm s^{-1} and a constant inter-track time delay of 50 µs.

5.2.1. Effect of overlap ratio on melt pool depth evolution

The evolution of the melt pool depth allows us to directly understand the influence of the overlap ratio on the stability and continuity of the melting process.

Table 2: Quantitative comparison of melt pool depth evolution for different overlap ratios

Overlap	Maximum melt pool depth (µm)	Mean depth (µm)	Increase vs. 0%
0%	109.46	93.02	—
10%	115.07	96.80	+4.1 %
20%	128.00	104.00	+11.8 %
30%	140.00	109.43	+17.6 %

The figures 8 to 11 illustrate the evolution of the melt pool depth during successive laser scans for different overlap ratio (0%, 10%, 20%, and 30%). The quantitative analysis summarized in table 2, clearly demonstrates that an increase in the coverage rate promotes a progressive widening of the melted area due to increased thermal interaction between adjacent scan tracks. The maximum melt pool depth increases from 109.46 µm at 0% coverage to 115.07 µm, 128.00 µm, and 140.00 µm for coverage rates of 10%, 20%, and 30%, respectively. Consequently, the average maximum melt pool depth increases from 93.02 µm to 109.43 µm, representing an overall increase of approximately 17.6% compared to the configuration without coverage.

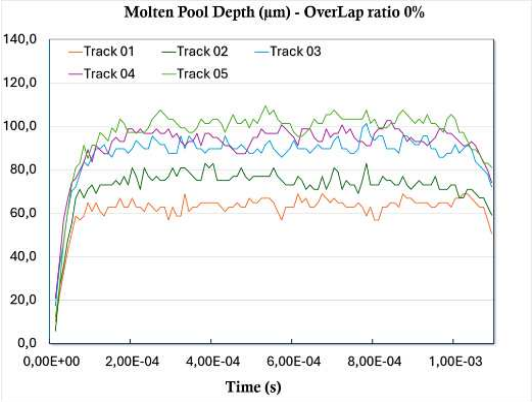


Figure 8: Evolution of melt pool depth for 0% overlap ratio

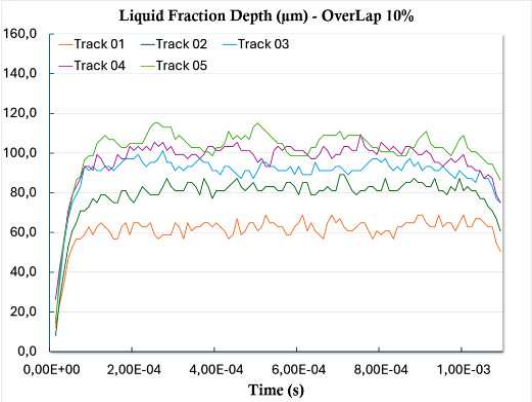


Figure 9: Evolution of melt pool depth for 10% overlap ratio

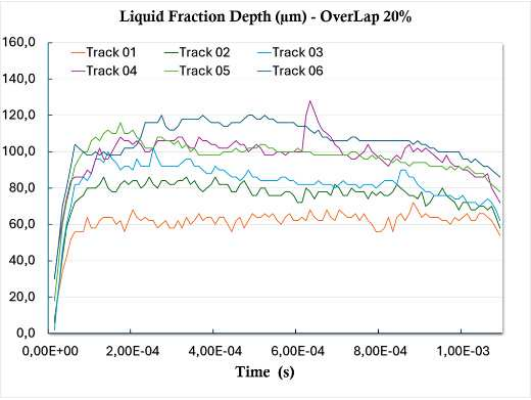


Figure 10: Evolution of melt pool depth for 20% overlap ratio

In a non-overlapping configuration (overlap ratio 0%, figure 8), each track behaves almost independently, with no geometric interaction between adjacent scan paths. Consequently, the depth of the melt pool gradually increases from the first to the last path, primarily due to the low heat accumulation generated indicating that the thermal influence of neighboring tracks remains limited, while the molten zone solidifies rapidly after each laser passes. With a 10% overlap ratio (figure 9), a small increase in the depth of the molten pool is observed for almost all tracks. Although the overall increase remains moderate (approximately 4.1% of the average maximum depth of 0% overlap ratio), the results indicate that the adjacent sweep passes already contribute to the partial preheating of the surrounding material, thus reducing heat loss and promoting deeper penetration. The configuration with overlap ratios of 20% and 30% (Figures 10 and 11) presents the deepest and unstable melt pool. Maximum penetration reaches 128 µm for a 20% overlap and 140 µm for 30%, while the maximum depth increases by approximately 11.8% and 17.6% for the 20% and 30% cases, respectively, compared to the configuration with no overlap (0%). Also, the differences between successive tracks decrease, indicating a more homogeneous thermal field generated by repeated laser exposure. This behavior suggests that thermal accumulation eventually dominates the melting process, resulting in a more unstable melt zone throughout the laser scanning.

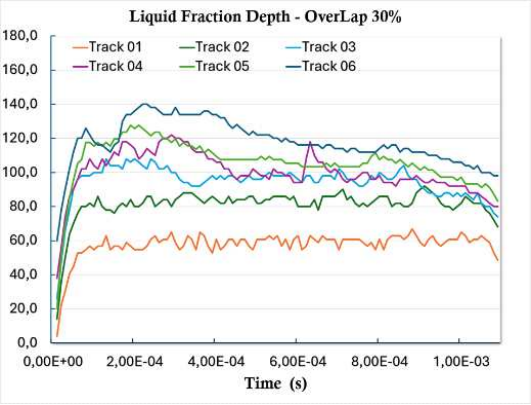


Figure 11: Evolution of melt pool depth for 30% overlap ratio

In addition, the thermal field provides a better understanding of melt pool stability. Increased overlap ratio enhances heat accumulation, resulting in a more uniform thermal field, a 35% to 45% increase in the depth of the molten pool, and an extended duration of the molten pool before solidification due to inter-track thermal interaction. These conditions improve the stability of the molten pool for intermediate overlaps (10%) by promoting controlled remelting and a stronger metallurgical bond between the tracks. However, with a 20% to 30% overlap ratios, excessive heat accumulation increases the volume of molten metal and prolongs solidification time, thus enhancing Marangoni convection and recoil pressure, resulting in an unstable keyhole regime. Although cooling rates remain on the order of 10^5 and 10^6 K s^{-1}, the prolonged lifetime of the molten pool increases the melt's susceptibility to oscillations, surface deformations, and pores formation. Consequently, the stability of the molten metal is governed by the balance between thermal homogenization and thermal gradients; an overlap of 10% provides the most favorable thermal conditions, whereas an overlap of 20% to 30% promotes hydrodynamic instability gas bubble illustrated in figure 12.

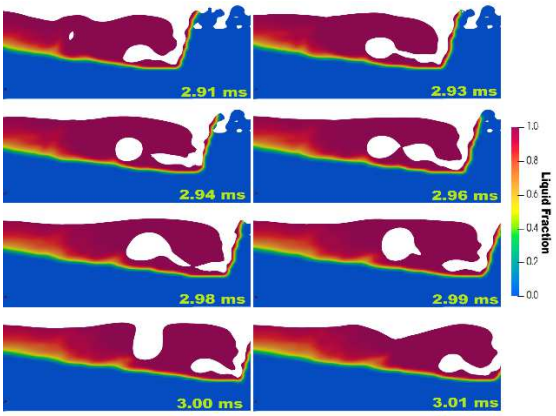


Figure 12: Transient hydrodynamic instability of gas bubble in molten pool.

Beyond these observations, the melt pool instability allows us a better understanding of the potential defect's formation as pores. At 0% overlap, isolated melt pools and rapid solidification ensure stable melting conditions, resulting in no pore formation. A 10% overlap promotes partial remelting and better adhesion between tracks, although localized transient instabilities (figure 13) can induce pores. At higher overlap ratios (20% and 30%), increased heat accumulation, prolonged melt pool lifetime, and higher thermal gradients increase its instability. These conditions promote unstable recoil pressure, intensified Marangoni convection, delayed solidification, and repeated remelting, thus

increasing growth pore formation and surface deformation. Therefore, although increased overlap ratio improves the continuity of the molten pool, excessive overlaps can compromise process stability through the formation of pores.

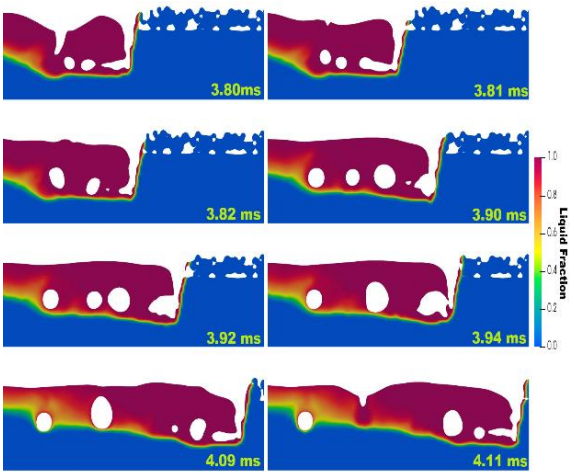


Figure 13: Pres mechanism formation by entrapped bubbles

Overall, the analysis of the liquid fraction demonstrates that an increase in the overlap ratio progressively changes the melting process, modifying from isolated melting zones to a thermally coupled multiple melting regime. However, the liquid fraction alone does not explain the physical mechanisms responsible for this evolution. A detailed analysis of the temperature evolution over time is therefore necessary to identify the effects of heat accumulation, remelting, and cooling kinetics.

5.2.2. Effect of overlap ratio on temperatures history and cooling kinetics

The temperature profile obtained from the numerical simulations provides a comprehensive description of the solidification behavior at three distinct points. The first point (point 1) was located at the center of the first track, the second one (point 2) at the center of the top surface of the substrate, and the third (point 3) at the center of the last track. The interpolation at liquidus (TL = 1923 K) and solidus (TS = 1878 K) temperatures revealed that the overlap ratio influences not only the cooling rate but also the occurrence of multiple melt-solidification cycles. This observation is one of the most significant results of this study, as it directly reflects the increasing thermal interaction between adjacent tracks.

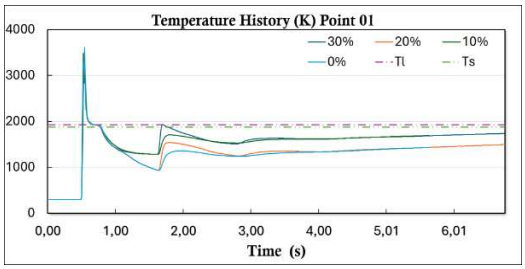


Figure 14: temperature history at point 1

At point 1 (figure 14), a single liquidus-solidus transition is observed for overlap ratios of 0%, 10%, and 20%, with cooling rates remaining almost constant between 6.920×10^5 and 7.481×10^5 K s^{-1}, corresponding to solidification times of 0.060 to 0.065 ms. This small variation indicates that the

thermal response of the first curve is mainly controlled by thermal conduction to the substrate, where thermal gradients favor relatively rapid cooling. In contrast, the 30% overlap configuration presents two successive liquidus-solidus transitions. The first solidification cycle (0.721–0.782 ms) induces a cooling rate of 7.307×10^5 K s^{-1}, while a second complete melt-solidification cycle (1.723–1.781 ms), caused by the reheating of adjacent tracks, produces a comparable cooling rate of 7.799×10^5 K s^{-1}. This behavior provides clear numerical evidence of complete remelting caused by the increased heat accumulation at the maximum overlap ratio.

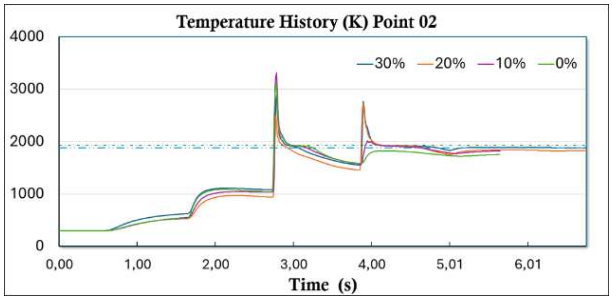


Figure 15: temperature history at point 2

At point 2 (figure 15), located near the center of the multi-track area, the influence of overlaps becomes more significant. With no overlap ratio (0%), a single melt-solidification cycle is observed, with an average cooling rate of 2.622×10^5 K s^{-1} and a solidification time of 0.172 ms, nearly three times longer than at point 1. This reflects reduced heat dissipation due to thermal interactions between adjacent tracks. In contrast, overlap rates of 10%, 20%, and 30% produce two successive melt-solidification cycles, corresponding to primary solidification followed by remelting induced by successive laser passes. For overlaps of 10% and 30%, the cooling rate decreases from 3.033×10^5 to 0.900×10^5 K s^{-1} and from 4.030×10^5 to 0.862×10^5 K s^{-1}, respectively, demonstrating that second solidification is approximately four to five times slower, with heat accumulation reducing the thermal gradient. The 20% overlap presents a distinct response, with a primary cooling rate of 1.002×10^6 K s^{-1} and a solidification time of 0.045 ms, indicating rapid heat extraction under a high thermal gradient before significant heat accumulation. After remelting, the cooling rate decreases to 1.125×10^5 K s^{-1} and the solidification time increases to 0.400 ms, thus slowing secondary solidification by a factor of nine. These two solidification regimes clearly demonstrate remelting and the progressive accumulation of heat during the fabrication of multi-track laser powder bed fusion (LPBF).

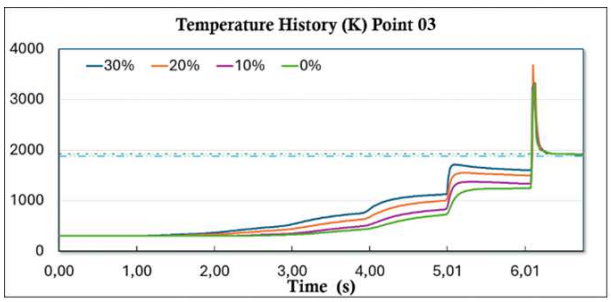


Figure 16: temperature history at point 3

Another important observation concerns point 3 in figure 16. For all overlap ratios, the temperature decreases below the liquidus temperature but does not reach the solidus temperature during the

simulation. Consequently, neither the solidification time nor the average cooling rate can be determined. This behavior is physically consistent: it indicates that the last deposited track remains in the mushy zone due to heat accumulation and thermal interactions with adjacent tracks. Complete solidification therefore occurs after the simulation time ends. Repeated liquidus-solidus transitions directly indicate remelting. The heat from successive scans remelts the previously solidified material, generating additional melt-solidification cycles with lower thermal gradients and longer solidification times.

As is well known, the cooling rate has a direct and significant effect on microstructural evolution (grain size and orientation), thereby determining the final mechanical properties of the manufactured part. Consequently, from a metallurgical perspective, the first solidification, which occurs at cooling rates of approximately 2.6×10^5 to 1.0×10^6 K s^{-1}, favors the formation of fine α′ martensite [31]. In contrast, remelting-solidification cycles occur at lower cooling rates (0.86×10^5 to 1.1×10^5 K s^{-1}), increasing the interaction time and favor grain growth, epitaxial growth of β grains, and the tempering or partial decomposition of the martensite. Consequently, remelting alters both the thermal history and the resulting microstructure [31].

Overall, increasing overlap changes the thermal history rather than simply reducing the cooling rate. At 0% overlap, only a single solidification event occurs. At 10%, secondary remelting appears, while 20% and 30% overlap produce increasingly extensive remelting, with thermal accumulation eventually affecting the entire deposited layer. These results demonstrate that overlap controls cooling kinetics, remelting frequency, and microstructural evolution [32], making it a key parameter governing the final properties of LPBF Ti-6Al-4V components.

5.3. Physical mechanisms governing thermal evolution on microstructure morphology

The evolution of the temperature field and the melt pool during the LPBF process is mainly governed by heat accumulation. This accumulation, due to the increased overlap ratio, limits heat dissipation in the substrate and surrounding powder. The resulting heat accumulation enhances remelting, prolongs the molten pool lifetime, and increases the melt pool depth, while simultaneously delaying solidification and reducing the average cooling rate, despite constant laser power and scan speed.

In addition, thermal accumulation alters the hydrodynamics of the melt pool by increasing metal evaporation, recoil pressure, and Marangoni convection resulting in the formation of keyhole which promotes multiple laser reflections, increasing energy absorption and enhancing remelting. While these combined effects improve melt pool continuity and adhesion between tracks at moderate overlap ratio, excessive heat accumulation destabilizes the melt pool, leading to keyhole collapse, gas trapping, surface deformation, and pore formation.

From a metallurgical perspective, rapid cooling at low overlaps ratio favors the formation of a fine α′ martensitic microstructure. As the overlap ratio increases, repeated thermal cycling and remelting promote epitaxial grain growth, reduce thermal gradients, and improve microstructural homogeneity. However, excessive thermal accumulation and prolonged liquid residence alter solidification conditions and melt pool stability, potentially modify grain morphology, residual stress distribution,

and local mechanical properties.

6. Conclusion

This work describes the influence of the overlap ratio on the thermal behavior and evolution of the melt pool during single and multi-track laser powder bed fusion, using a three-dimensional CFD model. Also, the study establishes the physical relationship between the thermal accumulation induced by the overlap ratio, remelting, and solidification. Increasing the overlap ratio by reducing hatch space between tracks enhances heat accumulation and limits heat dissipation. The resulting increase in residual temperature leads to the formation of deeper and longer-lived melt pools, repeated remelting, delayed solidification, and slower cooling rates. Simultaneously, the grew in thermocapillary flow, recoil pressure, and multiple laser reflections increases melt pool instability, causing a transition from stable at low-overlap ratio to an unstable regime at high-overlap ratio. The results identify overlaps ratio as a key parameter governing both microstructure and process stability. Moderate overlap improves inter-track fusion, whereas excessive overlap promotes thermal and hydrodynamic instability and increases the risk of process-induced defects. Overall, the study establishes a physical framework linking overlap ratio to thermal accumulation, melt pool evolution, and solidification, providing a basis for optimizing LPBF processing conditions while maintaining stable consolidation.

Despite the previous comprehensive understanding obtained in this study, the optimization of the LPBF process cannot depend only on single-track analyses. As successive laser tracks depending on overlap ratio parameter, increase thermal accumulation and melt pool interactions progressively dominate the process, highlighting the need for multi-track and ultimately multi-layer investigations. Effectively, although single-track simulations are essential for understanding laser-material interaction and validating numerical models, they cannot apprehend the thermal accumulation interactions occurring during realistic fabrication process. However, multi-track simulations remain an intermediate study because they neglect thermal accumulation along the build direction. During LPBF, each deposited layer is formed on a substrate whose thermal state is inherited from previous layers. Extending the present approach to multi-layer simulations is therefore essential to establish a predictive framework capable of describing heat accumulation and defect formation in build direction. Also to improve a complete study and optimization of the process, it’s essential to model the microstructure evolution and the resulting mechanical properties, using the datas obtained from the present CFD model as an input’s parameters.

Declarations

Ethical Approval

Not applicable. This study did not involve human participants, human biological materials, or animal experiments.

Funding

The authors received no external funding for this research.

Availability of Data and Materials

The data supporting the findings of this study are available from the corresponding author upon reasonable request.

References:

[1] D. Gu, M. Xia, and D. Dai, "On the role of powder flow behavior in fluid thermodynamics and laser processability of Ni-based composites by selective laser melting," International Journal of Machine Tools and Manufacture, Article vol. 137, pp. 67-78, 2019

[2] Kelbel, H.C.; Stoecker, L.; Frank, J.J.; Lukas, G.; Bergweiler, G.; Gries, T.; Greb, C.; Schuh, G. Applicability of Advanced Manufacturing Technologies for Agile Product Development in the Internet of Production: A Strategic Framework. J. Prod. Syst.Logist. 2022, 2, 1–19.

[3] Nalivaiko, A.Y.; Ozherelkov, D.Y.; Pelevin, I.A.; Chernyshikhin, S.V.; Medvedev, A.E.; Korshunov, A.V.; Arnautov, A.N.; Gromov, A.A. Comprehensive Study of the 3D Printing of Single Tracks and Cubic Samples by Selective Laser Melting of AlSi10MgCu Alloy. Met. Mater. Int. 2022, 28, 787–801. [CrossRef]

[4]. Ahmed, A.; Wahab, M.S.; Raus, A.A.; Kamarudin, K.; Bakhsh, Q.; Ali, D. Effects of Selective Laser Melting Parameters on Relative Density of AlSi10Mg. Int. J. Eng. Technol. 2016, 8, 2552–2557.

[5] Colomo, A.G.; Wood, D.; Martina, F.; Williams, S.W. A comparison framework to support the selection of the best additive manufacturing process for specific aerospace applications. Int. J. Rapid Manuf. 2020, 9, 194.

[6] Jalali, M.; Mohammadi, K.; Movahhedy, M.R.; Karimi, F.; Sadrnezhaad, S.K.; Chernyshikhin, S.V.; Shishkovsky, I.V. SLM Additive Manufacturing of NiTi Porous Implants: A Review of Constitutive Models, Finite Element Simulations, Manufacturing, Heat Treatment, Mechanical, and Biomedical Studies. Met. Mater. Int. 2023, 29, 2458–2491.

[7] Bassoli, E.; Defanti, S.; Tognoli, E.; Vincenzi, N.; Degli Esposti, L. Design for Additive Manufacturing and for Machining in the Automotive Field. Appl. Sci. 2021, 11, 7559.

[8] U. Scipioni Bertoli, G. Guss, S. Wu, M. J. Matthews, and J. M. Schoenung, "In-situ characterization of laser-powder interactionand cooling rates through high-speed imaging of powder bed fusion additive manufacturing," Materials and Design, Article vol. 135, pp. 385-396, 2017, doi: 10.1016/j.matdes.2017.09.044.

[9] Tseng, C.-C. and C.-J. Li, Numerical investigation of interfacial dynamics for the melt pool of Ti-6Al-4V powders under a selective laser. International Journal of Heat and Mass Transfer, 2019. 134: p. 906-919.

[10] Verhaeghe, F., et al., A pragmatic model for selective laser melting with evaporation. Acta

Materialia, 2009. 57(20): p. 6006-6012.

[11] Xia M, Gu D, Yu G, Dai D, Chen H, Shi Q. Porosity evolution and its thermodynamic mechanism of randomly packed powder-bed during selective laser melting of Inconel 718 alloy. Int J Mach Tool Manufact 2017;116:96e106.

[12] Monroy K, Delgado J, Ciurana J. Study of the pore formation on CoCrMo alloys by selective laser melting manufacturing process. Procedia Eng 2013;63:361e9.

[13] Markl, M.; Körner, C. Multiscale Modeling of Powder Bed-Based Additive Manufacturing. Annu. Rev. Mater. Res. 2016, 46, 93–123.

[14] Soundararajan, B.; Sofia, D.; Barletta, D.; Poletto, M. Review on modeling techniques for powder bed fusion processes based on physical principles. Addit. Manuf. 2021, 47, 102336.

[15] Cook, P.S.; Murphy, A.B. Simulation of melt pool behaviour during additive manufacturing: Underlying physics and progress. Addit. Manuf. 2020, 31, 100909.

[16] Körner, C.; Attar, E.; Heinl, P. Mesoscopic simulation of selective beam melting processes. J. Mater. Process. Technol. 2011, 211, 978–987.

[17] King, W.; Anderson, A.; Ferencz, R.; Hodge, N.; Kamath, C.; Khairallah, S.; Rubenchik, A. Laser powder bed fusion additive manufacturing of metals; physics, computational, and materials challenges. Appl. Phys. Rev. 2015, 2, 041304.

[18] Chernyshikhin, S.V.; Firsov, D.G.; Shishkovsky, I.V. Selective Laser Melting of Pre-Alloyed NiTi Powder: Single-Track Study and FE Modeling with Heat Source Calibration. Materials 2021, 14, 7486.

[19] M. Bayat et al. (2019) Keyhole-induced porosities in Laser-based Powder Bed Fusion (L-PBF) of Ti6Al4V: High-fidelity modelling and experimental validation. Additive Manufacturing, 30 (2019).

[20] Khairallah, S.A., et al. (2016) Laser Powder-Bed Fusion Additive Manufacturing: Physics of Complex Melt Flow and Formation Mechanisms of Pores, Spatter and Denudation Zones. Acta Materialia, 108, 36-45.

[21] Khairallah, S.A., et al. (2020) Controlling interdependent meso-nanosecond dynamics and defect generation in metal 3D printing, Science, 2020 May 8;368(6491):660-665.

[22] Haodong Chen et al. Revealing formation mechanism of end of process depression in laser powder bed fusion by multi-physics meso-scale simulation, Virtual and Physical Prototyping, March 2024, 19(1)

[23] A. Chouhan et al. Role of melt flow dynamics on track surface morphology in the L-PBF additive manufacturing process, International Journal ofHeatandMassTransfer178(2021) 121602

[24] Thongpron et al (2024), Effect of hatch spacing in selective laser melting process of Ti-6Al-4V alloy on finished surface roughness: A computational study. 2024, Journal of Metals Materials and Minerals 34(3) :1861

[25] Chen Liu et al. Simulation Study on the Impact of Melt Track Overlap Rate on the Forming Result During the Selective Laser Melting of Ti-6Al-4V Alloy. Materials 2025, 18(10), 2314

[26] A.J.I. Bagasol, et al. “Ti-6Al-4V alloy printing — correlations between experimental and numerical modelling melt pool data.” The International Journal of Advanced Manufacturing Technology, vol. 133, 2024, pp. 3603–3617.

[27] J. Katagiri, et al “Influence of recoil pressure, mushy zone flow resistance and reflectivity on melt pool shape in laser powder bed fusion simulation”, Case Studies in Thermal Engineering, Vol. 50, 2023, pp 103477.

[28] M. Mohammad et al. “Laser powder bed fusion of Ti-6Al-4V parts: Thermal modeling and mechanical implications”, International Journal of Machine Tools and Manufacture, Vol. 118–119, 2017, pp 73-90.

[29] C. Ransenigo et al. “Evolution of Melt Pool and Porosity During Laser Powder Bed Fusion of Ti6Al4V Alloy: Numerical Modelling and Experimental Validation.” Lasers in Manufacturing and Materials Processing, 9, 481–502, 2022.

[30] A. Samaei et al. “Benchmark Study of Melt Pool and Keyhole Dynamics, Laser Absorption, and Porosity in Additive Manufacturing of Ti-6Al-4V.” NIST, 2024.

[31] N. Derimow et al. “Investigation of melt pool dynamics and solidification microstructures of laser melted Ti-6Al-4V powder using X-ray synchrotron imaging.” NIST, 2024.

[32] L. Nastac “A 3D Multiscale Model for Prediction of the Microstructure Evolution in Ti6Al4V Components Produced by Laser Powder Bed Fusion” IOP Conference Series: Materials Science and Engineering, 2023, Vol 1281, pp 012002